# Adsorption of Maleic Acid Monomer on the Surface of Hydroxyapatite and TiO$_2$: A Pathway toward Biomaterial Composites

Mitchell Albert, Amanda Clifford, Igor Zhitomirsky,* and Oleg Rubel*⊙

Department of Materials Science and Engineering, McMaster University, 1280 Main Street West, Hamilton, Ontario L8S 4L8, Canada

ABSTRACT: Poly(styrene-*alt*-maleic acid) adsorption on hydroxyapatite and TiO$_2$ (rutile) was studied using experimental techniques and complemented by ab initio simulations of adsorption of a maleic acid segment as a subunit of the copolymer. Ab initio calculations suggest that the maleic acid segment forms a strong covalent bonding to the TiO$_2$ and hydroxyapatite surfaces. If compared to vacuum, the presence of a solvent significantly reduces the adsorption strength as the polarity of the solvent increases. The results of first-principles calculations are confirmed by the experimental measurements. We found that the adsorbed poly(styrene-*alt*-maleic acid) allowed efficient dispersion of rutile and formation of films by the electrophoretic deposition. Moreover, rutile can be codispersed and codeposited with hydroxyapatite to form composite films. The coatings showed an enhanced corrosion protection of metallic implants in simulated body fluid solutions, which opens new avenues for the synthesis, dispersion, and colloidal processing of advanced composite materials for biomedical applications.

KEYWORDS: *maleic acid monomer, hydroxyapatite, rutile, surface adsorption, density functional theory, electrophoretic deposition, coating, corrosion protection*
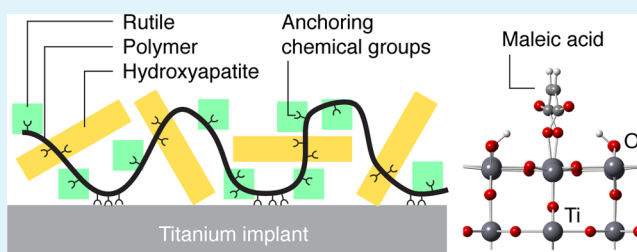
1. INTRODUCTION

Investigations of adsorption of organic molecules at the surface of nanomaterials and their colloidal behavior[1] allowed for the development of novel strategies for the surface modification, dispersion, and advanced synthesis of nanoparticles. Studies of mussel adsorption on inorganic surfaces[2,3] provide important chemical and physical insights into development of covalent anchoring mechanisms. It was found that the strong mussel adhesion involves protein macromolecules that contain a catecholic amino acid L-3,4-dihydroxyphenylalanine (L-DOPA). The adhesion mechanism of mussels is attributed to the complexation or bridging bidentate bonding between metal atoms on material surfaces and hydroxyl groups of catechol.[4] These studies have generated interest in the investigation of catecholates and inspired the development of advanced adhesives,[3,5] dispersants,[6] and liquid−liquid extraction agents[7−10] containing anchoring catechol groups for various applications (see ref 11 and references therein).

The success in the applications of chelating molecules from the catechol family has driven investigations of natural aliphatic compounds with carboxyl groups, which can provide strong chelating or bridging polydentate bonding to inorganic materials. Of particular interest are fumaric and maleic acid (MA) isomers, containing trans and cis carboxyl groups, respectively. These acids showed strong adsorption on various oxides.[12] The cis conformation of MA provides an ideal orientation for coordination via both carboxylate groups in a strong tetradentate interaction.[12,13] It is in this regard that many dispersant molecules described in the literature provide a relatively weak monodentate bonding to the particle surface.[6,14−17] Clearly, tetradentate interactions of MA with oxide surfaces offer advantages for surface modification of materials.

Significantly stronger interactions with inorganic surfaces can be expected using MA polymers or copolymers. The individual MA monomers of such polymers can provide multiple chemical bonds with substrates. Poly(maleic acid) showed a strong adsorption on alumina particles and allowed for their efficient dispersion.[18] Poly(acrylic acid-*co*-maleic acid) exhibited a strong affinity to BaTiO$_3$ and clay minerals.[19,20] The adsorption properties of the poly(styrene-*alt*-maleic acid) (PSMA-h) copolymer (Figure 1) have been utilized for the synthesis of inorganic particles with different morphologies[21−23] and unusual superstructures.[24] PSMA-h is a biocompatible polymer, which is currently under investigations for many biomedical applications, such as drug delivery,[25−27] biosensors,[28] antimicrobial materials,[29] and implants.[30,31] PSMA-h demonstrated a strong affinity to hydroxyapatite (HA), bioglass, and bioceramics and allowed their electrophoretic deposition (EPD) and codeposition with proteins.[32] Colloidal techniques, such as EPD, have a high potential in the
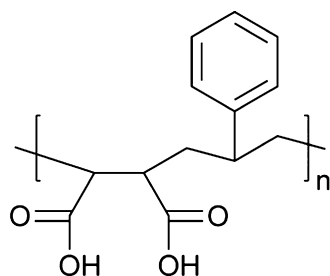
Figure 1. Styrene-MA copolymer.

development of advanced films, coatings, scaffolds, and devices for biomedical applications. Therefore, the investigation of PSMA-h adsorption on bioceramics opens new avenues for the synthesis, dispersion, and colloidal processing of advanced materials for biomedical applications.

HA is an important material for biomedical implant applications because its chemical composition is similar to that of natural bone.[33] Rutile is also known as a bioactive material, which promotes HA biomineralization.[34−36] Compared to the anatase phase, the rutile phase of TiO_2 has many advantages for implant applications, such as phase stability, chemical stability, and improved corrosion protection.[37] The addition of rutile to the HA to form a composite coating offers many benefits, such as enhanced chemical stability, improved corrosion protection of implants, bioactivity, improved mechanical properties, enhanced osteoblast adhesion, and cell growth.[38−42] Previous investigations[32] showed that HA coatings can be deposited by EPD using PSMA-h as a charging and dispersing agent, which strongly adsorbed on the HA surface.

The goal of this investigation was to probe the PSMA-h adsorption on HA and TiO_2 (rutile) using experimental techniques as well as to perform ab initio simulations of adsorption of a MA segment as a subunit of the copolymer. We identified the most stable TiO_2 and HA surfaces and their reconstructions in the presence of a solvent using first-principles atomistic modelling. We examined the molecular mechanisms and adsorption strength of MA on different surfaces of TiO_2 and HA. Our simulations indicate that two carboxylate functional groups of MA form strong covalent bonds at the surfaces of HA and TiO_2. In these calculations, MA was treated as a segment of a polymer chain rather than a monomer. Our studies demonstrate that a solvent significantly alters the surface energy and adsorption characteristics of molecules. Experimental measurements are performed to test the validity of the theory. The measurements include the use of PSMA-h as a dispersion agent for rutile and formation of films

by EPD. We examined the deposition yield, film morphology, and corrosion resistance. The possibility of codispersing and codepositing the rutile with HA to form composite films is investigated for biomedical applications.

2. METHODS

2.1. Computational Methods. The first-principles electronic structure calculations have been performed in the framework of the density functional theory (DFT)[43] using Perdew−Burke−Ernzerhof generalized gradient approximation (GGA-PBE) for the exchange−correlation functional.[44] The Vienna ab initio simulation program (VASP) and projector augmented-wave potentials[45−47] were used. Full self-consistent structural optimization was performed for the bulk TiO_2 (rutile) and HA. The structure was considered to be optimized when the magnitude of Hellmann−Feynman forces acting on atoms dropped below 10 meV/Å and components of the stress tensor did not exceed 1 kbar. The Brillouin zone was sampled using $3 \times 3 \times 4$ and $2 \times 2 \times 4$ Monkhorst−Pack grids[48] for TiO_2 and HA primitive cells, respectively. The cutoff energy for a plane wave expansion was set at 500 eV, which is 25% higher than the value recommended in the pseudopotential file for oxygen. The higher cutoff energy was essential for obtaining accurate structural parameters, which are summarized in Table 1. The theoretical lattice parameters are within 2% error of the experimental values, which is typical for GGA-PBE. An attempt was made to include the on-site Coulomb interaction for Ti d-electrons in the framework of Dudarev et al.[49] using an effective Hubbard energy of $U = 2$ eV.[50] However, this correction resulted in a greater deviation between theoretical and experimental lattice parameters and thus was abandoned.

$TiO_2(110)$ and HA(0001) and $(01\bar{1}0)$ surfaces are obtained on the basis of the optimized bulk structures. The 20 Å spacing between periodical images of slabs in a direction perpendicular to the surface ensures no spurious interactions. The $TiO_2(110)$ slab is represented by four monolayers of Ti atoms with a well-established surface termination that consists of alternating rows of 5- and 6-fold-coordinated Ti sites running along the [001] direction.[53,54] The HA(0001) and $(01\bar{1}0)$ slabs are constructed using nine and seven monolayers of Ca atoms, respectively. There are some ambiguities about the HA$(01\bar{1}0)$ surface and its reconstruction.[55−57] Several scenarios for a stoichiometric cleavage surface were explored. The lowest surface energy corresponds to the cleavage plane selected such that PO_4 tetrahedra remain preserved (Figure 2). It is this surface reconstruction that is later used for studying the adsorption of molecules. Atoms of the slab representing the surface were allowed to relax except for three monolayers in the center of the slab that were constrained to the bulk atomic positions. The presence of a solid−liquid interface is modeled using an implicit solvation model implemented in VASPsol[58] and values of the static dielectric constant for a water−ethanol mixture tabulated in ref 59.

The MA molecular structure (Figure 3a,b) is obtained by relaxing all degrees of freedom in a simulation box of the size $15 \times 15 \times 15$ Å³ to prevent spurious interactions between periodical images. However, this molecule is not chemically equivalent to the MA being a segment of the copolymer. To model the MA segment, two hydrogen-

Table 1. Bulk Structure Properties (Lattice Parameters and Fractional Coordinates of Atoms) of TiO_2 and HA[a]

compound	calculated			experiment		
	$a = b$ (Å)	c (Å)	u	$a = b$ (Å)	c (Å)	u
TiO_2 (rutile)	4.664	2.966	O (0.3046, 0.3046, 0)	4.594	2.959	O (0.3048, 0.3048, 0)
hydroxyapatite	9.549	6.934	Ca_I (1/3, 2/3, 0.0016)	9.432	6.881	Ca_I (1/3, 2/3, 0.0014)
			Ca_{II} (0.2501, 0.9986, 0.2513)			Ca_{II} (0.2466, 0.9931, 1/4)
			P (0.3988, 0.3682, 0.2524)			P (0.3982, 0.3682, 1/4)
			O_I (0.3301, 0.4850, 0.2538)			O_I (0.3283, 0.4846, 1/4)
			O_{II} (0.5877, 0.4638, 0.2470)			O_{II} (0.5876, 0.4652, 1/4)
			O_{III} (0.3379, 0.2549, 0.0737)			O_{III} (0.3433, 0.2579, 0.0705)

[a]Theoretical results are obtained using DFT. The neutron diffraction experimental data for TiO_2 and HA are taken from refs 51 and 52.
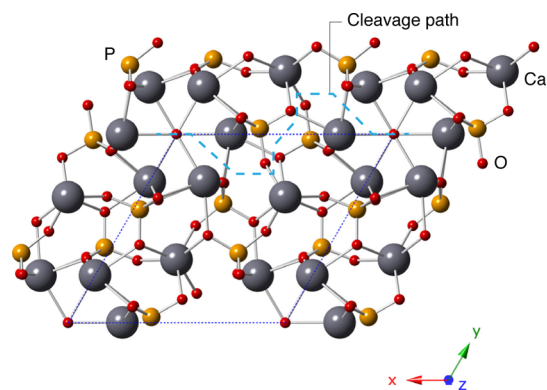
Figure 2. HA low-energy $(01\bar{1}0)$ stoichiometric surface is created by cleaving the slab along the dashed line. The construction maintains the integrity of PO_4 tetrahedra.
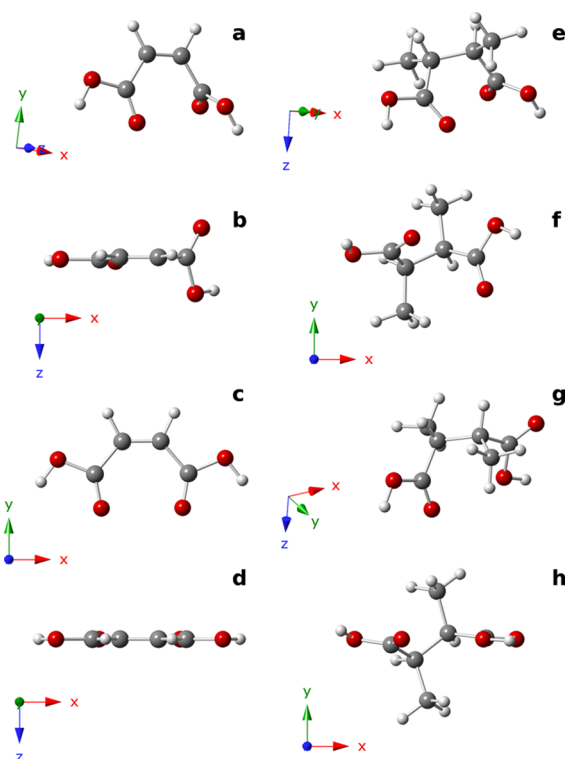

Figure 3. Structure of MA as a monomer (a,b) 3D conformer, (c,d) 2D flattened conformer and as a part of the polymer chain, (e,f) 3D conformer, and (g,h) 2D flattened carboxyl groups. The deformation energy associated with changing the conformation 3D → 2D is approximately 0.15 eV.

terminated carbon atoms were added to the MA molecule such that they mimic a polymer chain (Figure 3e,f). As a result, the sp^2 double bond between two carbon atoms in MA transforms into an sp^3 single bond in the MA segment. It is assumed that the individual MA segment can represent an MA residue as a part of copolymer and can serve as a basis for studying its adsorption at inorganic surfaces. This choice is driven by the necessity to make our model computationally feasible at the first-principles level. At the same time, we admit that this approach omits some details of the copolymer conformation that can limit the exposure of MA residues to the solvent/surface and possible interactions between phenyl group and the surfaces.

The adsorption of MA monomer and MA segment is modeled as an inner-sphere surface complex. The molecules were initially positioned at the surface in such a way that the distance and arrangement between the metal ion and oxygen atoms of the ligands

resembles that in the bulk. The structural optimization is performed until Hellmann–Feynman forces acting on atoms dropped below 20 meV/Å. Crystallographic information files (CIFs) with atomic structures used in calculations can be accessed through the Cambridge crystallographic data centre (CCDC deposition numbers 1582972–1582992).

2.2. Experimental Section. Titanium foil (0.127 mm), TiO_2 (rutile, particle size less than 100 nm), PSMA-h, $Ca(NO_3)_2\cdot4H_2O$, $(NH_4)_2HPO_4$, NH_4OH, and Hank's balanced salt solution ($CaCl_2$ 0.14 g L^{-1}, KCl 0.40 g L^{-1}, KH_2PO_4 0.06 g L^{-1}, $MgCl_2\cdot6H_2O$ 0.10 g L^{-1}, $MgSO_4\cdot7H_2O$ 0.10 g L^{-1}, NaCl 8.00 g L^{-1}, $NaHCO_3$ 0.35 g L^{-1}, Na_2HPO_4 0.048 g L^{-1}, glucose 1.00 g L^{-1}, and phenol red 0.01 g L^{-1}, Sigma-Aldrich, Canada) were used for the following experiments. Stoichiometric HA was synthesized using wet chemical precipitation, by the slow addition of 0.6 M $(NH_4)_2HPO_4$ solution to 1.0 M $Ca(NO_3)_2$ solution while continuously stirring at 70 °C. The solution was stirred for 8 h at 70 °C, followed by 24 h of stirring at room temperature, and the pH was adjusted to 11 using NH_4OH. The resulting precipitate was washed using water and ethanol and then dried. Crystalline needle-shaped HA nanoparticles have been obtained using this method. The transmission electron microscopy (TEM) micrograph presented in Figure 4 shows a needle-shaped HA particle morphology. HA particles had an aspect ratio of approximately eight and an average length of 150 nm.
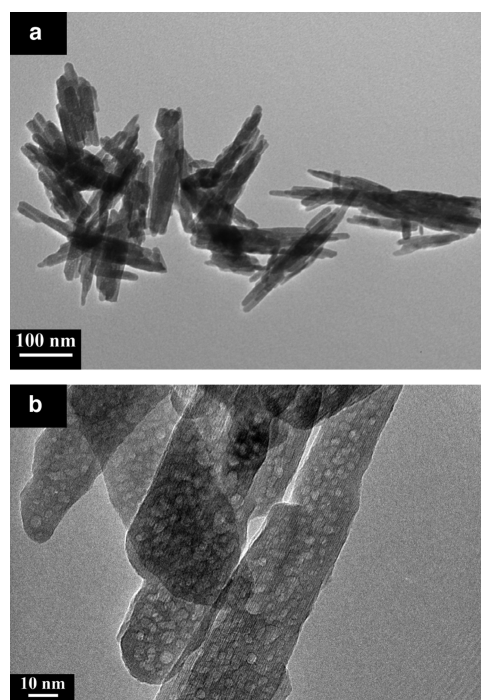
Figure 4. TEM images of hydroxyapatite particles at two different magnifications: (a) ×150 000 and (b) ×10⁶.

Stainless steel or titanium foil was used as substrates for EPD. The substrate was placed 15 mm away from the platinum counter electrode. The deposition time was varied in the range of 1–6 min, and deposition voltage was within the range of 10–15 V. TiO_2 and HA were dispersed in a mixed water–ethanol solvent (40% water), containing dissolved PSMA-h. The use of the mixed solvent offered the advantage of reduced gas evolution at the substrate surface. The deposition yield was studied using stainless steel substrates. Potentiodynamic studies were performed using a PARSTAT 2273 potentiostat and the PowerSuite software (Princeton Applied Research). A three-cell electrode cell was used for electrochemical testing, with a saturated calomel electrode as the reference electrode and platinum mesh as the counter electrode. The test was carried out in Hank's balanced salt solution, which was used to simulate

physiological conditions. A scan rate of 1 mV/s was used to obtain the potentiodynamic polarization curves.

A JEOL 7000F scanning electron microscope and an FEI Tecnai Osiris transmission electron microscope were used for electron microscopy. A Nicolet I2 diffractometer with monochromatized Cu Kα radiation was used for X-ray diffraction (XRD). Fourier-transform infrared (FTIR) spectroscopy studies were performed on a Bruker Vertex 70 spectrometer.

3. RESULTS AND DISCUSSION

We begin with examining surfaces of rutile and HA. The specific surface energy is defined as

$$\gamma = \frac{E_{tot}(slab) - E_{tot}(bulk)}{2A} \qquad (1)$$

where E_{tot} is the DFT total energy of the slab and the bulk material, A is the planar surface area, and the factor of 2 accounts for the presence of two surfaces at the top and bottom of the simulation slab. Results for the surface energy are presented in Table 2, which also includes the values of the

Table 2. Calculated Surface Energy and Absorption Energy of MA at TiO$_2$ and HA Surfaces[a]

surface	surface energy (J/m^2)	adsorption enthalpy (eV)	
		monomer	segment
TiO$_2$(110)	0.63[b]/0.48/0.44	−1.3/−0.7/−0.6	−1.3/−0.9/−0.6
HA(0001)	0.90[c]/0.53/0.45	−3.4/−1.3/−1.2	
HA(01$\bar{1}$0)	0.96[d]/0.59/0.51	−4.7/−2.5/−2.1	−4.0/−1.8/−1.5

[a]Values are presented for various solvent conditions: vacuum/mixture 80% ethanol + 20% water/100% water, respectively. [b]0.31−0.47, 0.89 J/m^2 (DFT calculations[53,60]). [c]0.33, 0.77, 1.01, 1.93 J/m^2 (DFT calculations[55−57,61]). [d]0.33, 1.32, 1.36, 2.10 J/m^2 (DFT calculations[55−57,61]).

surface energies reported in the literature for comparison. A large scattering of literature values, in particular for HA, can be attributed to the variability in DFT approximations for the exchange−correlation functional, selection of pseudopotentials, and uncertainties in the structure specifically for the HA(01$\bar{1}$0) surface. HA has a higher surface energy that correlates with its higher wettability in comparison to TiO$_2$. The presence of a polar solvent (water) significantly affects the surface energy, in particular for HA. The disparity between the surface energies of TiO$_2$ and HA vanishes in the solvent.

The MA molecule and MA segment adapt a three-dimensional structure as shown in Figure 3a,b and e,f,

respectively. Some adsorption configurations require a structural deformation (flattening) of the MA molecule or MA segment. The flattening occurs via rotating the carboxyl groups to align both groups to a common plane, as illustrated in Figure 3c,d and g,h, respectively. The associated deformation energy is on the order of 0.15 eV as evaluated by DFT calculations, which is 1 order of magnitude less than typical adsorption energies. The ability of MA to easily adapt its structure to the surface of interest can be attributed to its aliphatic nature.

Figure 5 shows the lowest energy configuration of the MA monomer adsorbed on TiO$_2$ and HA surfaces. Adsorption to the TiO$_2$ surface takes place via an inner-sphere bonding to a pair of Ti atoms (a bridge bidentate coordination), as illustrated in Figure 6a, rather than chelate bidentate bonding to a single Ti site at the surface. This result can be explained by a dense packing of Ti atoms at the TiO$_2$ surface and is reminiscent of catecholate adsorption on TiO$_2$.[11,62] In the case of HA, the spacing between Ca atoms at the surface is too large. Therefore, chelation is a preferable type of bonding on HA (Figure 6b,c). The adsorption of MA is accompanied by deprotonation of both carboxyl groups. Those protons are readily attracted to passivate oxygen dangling bonds at the surface PO$_4$ tetrahedra and to restore the charge balance perturbed by the newly formed Ti−O or Ca−O bonds.[62] Regarding H$^+$ placement on the HA(01$\bar{1}$0) surface, there are several alternatives to the top of PO$_4$ tetrahedra, which include O atoms in the base of PO$_4$ tetrahedra as well as the $\equiv$Ca$_2$OH^{q-} groups present at the surface. It turns out that $\equiv$Ca$_2$OH$_2^{1-q}$ is the second most favorable scenario from the DFT total energy point of view.

The affinity of MA to the surfaces is characterized by the adsorption enthalpy, which is defined as

$$\Delta H_{ads} \approx E_{tot}(MA\ ads.\ ) - E_{tot}(MA) - E_{tot}(slab) \qquad (2)$$

where $E_{tot}(MA\ ads.)$ is the total energy of a slab with the molecule adsorbed on its surface (Figure 5), $E_{tot}(MA)$ is the total energy of the molecule or segment in its ground state configuration (Figure 3a or e), and $E_{tot}(slab)$ is the energy of the slab. The approximate sign reflects neglecting a zero-point energy change upon adsorption and finite temperature effects. This approximation is justified in an earlier study of catalytic reactions[63] because the sum of zero-point energies is approximately constant during the traversing of regions with energy barriers.

The adsorption enthalpies of MA on TiO$_2$ and HA surfaces are summarized in Table 2. Here, we list the results obtained
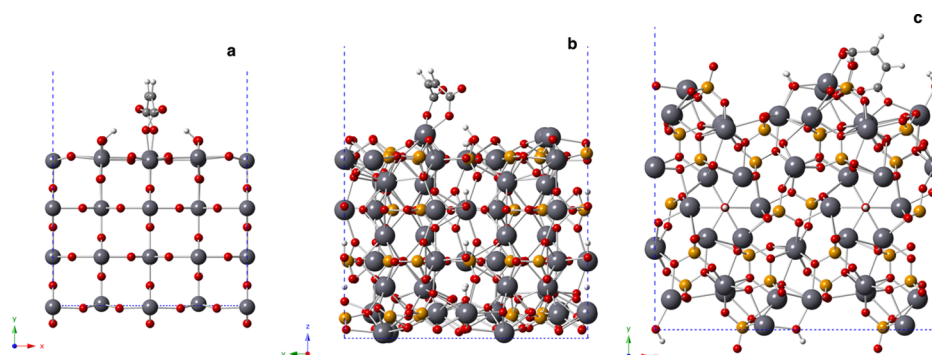
Figure 5. (a) Maleic acid monomer at the (110) surface of TiO$_2$, (b) at the HA(0001) surface, and (c) at the HA(01$\bar{1}$0) surface.
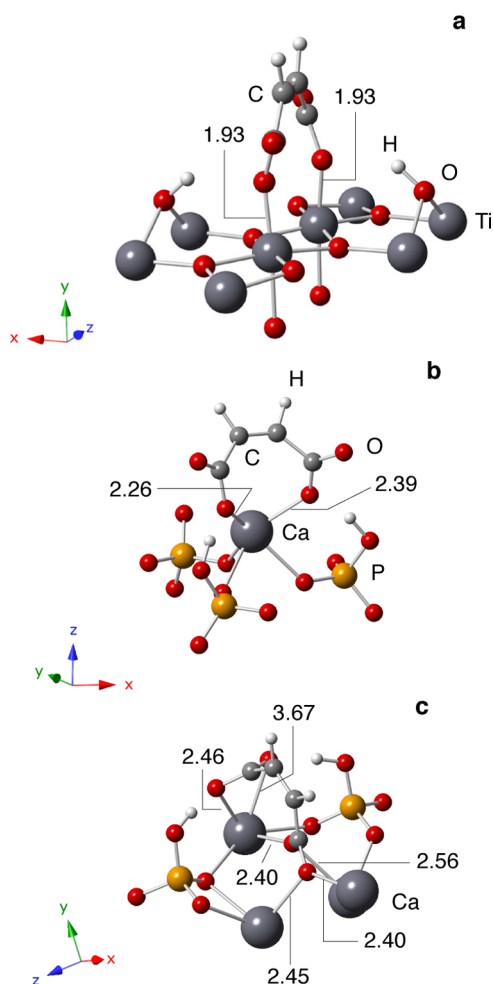
Figure 6. Maleic acid and neighbor atoms of the adsorption complex (a) at the (110) surface of TiO_2, (b) at the HA(0001) surface, and (c) at the HA(01$\bar{1}$0) surface. Bond distances between the MA and surface metal atoms are shown in Angstroms for an aqueous environment.

for different solvents (water and a mixture of water and ethanol) as well as for the vacuum because effects of the solvent are often neglected in studies of a molecular adsorption. The values of the adsorption enthalpy in Table 2 suggest that the binding energies of molecules to the surface are significantly overestimated in vacuum (almost by a factor of 2). The more ionic the solvent, the weaker the affinity of MA to the surface. The adsorption enthalpies of MA on TiO_2 and HA surfaces in water remain strong: ΔH_{ads} = −0.6 and −1.5 eV, respectively, in spite of solvation effect. The values are comparable to −1 eV bond strength between DOPA and Si surface measured experimentally,[64] the theoretical range from −1.1 to −1.3 eV for the TiO_2−dopamine bond strength,[65] and −1.5 eV for the caffeic acid adsorption on TiO_2 in vacuum.

Effect of the solution pH on adsorption energies can be accounted for by evaluating a change in the free energy of a residue as a result of deprotonation:[66]

$$\Delta G = -RT \ln 10(pH - pK_a) \qquad (3)$$

where R is the gas constant, T is the temperature, and pK_a is a dissociation constant. The dissociation constants for MA are pK_{a1} = 1.9 and pK_{a2} = 6.0.[67] This implies that both carboxyl groups are deprotonated at the experimental conditions (pH =

7). As a result, the free energy of MA is lowered by $\Delta G \approx$ −0.16 eV per residue (−0.10 and −0.06 eV for the first and second groups, respectively). To account for deprotonation, the magnitude of adsorption enthalpies in Table 2 should be corrected by the corresponding value of ΔG, which results in a reduction of the magnitude of the adsorption energy with increasing pH value but does not prevent MA residues from adsorption as observed experimentally by Hidber et al.[4]

Next, we continue with an experimental verification of theoretical predictions. It should be emphasized once again that individual MA monomers are used in the modeling section for the sake of computational simplicity, whereas PSMA-h copolymers are employed in the experimental section to provide multiple chemical bonds with substrates. Because of the limitations of the concept of zeta potential for analysis of particles, containing adsorbed polyelectrolytes,[68−70] the influence of PSMA-h adsorption on the electrokinetic behavior of the TiO_2 (rutile) particles was analyzed using the EPD yield data. The EPD experiments performed with 5−10 g L^{-1} TiO_2 (rutile) suspensions without PSMA-h showed the formation of cathodic deposits. The low cathodic EPD yield indicated that particles were weakly positively charged. PSMA-h films were deposited anodically and showed strong adhesion to the substrates. The film adhesion corresponded to 5B classification (ASTM D3359). The addition of PSMA-h to the TiO_2 suspensions resulted in a significant improvement of the suspension stability and the formation of anodic deposits. The formation of anodic films signified a particle charge reversal due to the adsorption of the negatively charged PSMA-h. The deposit mass increased with increasing deposition time at a constant applied voltage (Figure 7). The experimental results
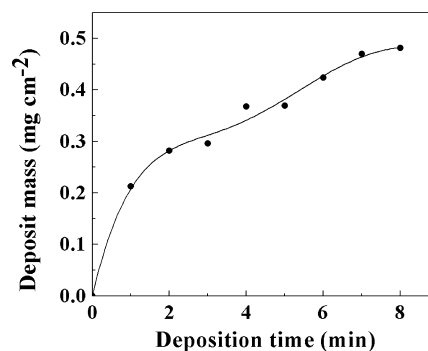

Figure 7. Deposit mass vs deposition time for 5 g L^{-1} TiO_2 suspension, containing 10 g L^{-1} PSMA-h at a deposition voltage of 15 V.

indicated that the film thickness can be controlled and varied. The deposition yield data showed a relatively high deposition rate. A decrease of deposition rate with time was observed because of the reduction in the voltage drop in the bulk of the suspension as a result of the formation of an insulating film layer on the electrode surface.

The PSMA-h adsorption on the TiO_2 particles was confirmed by the FTIR analysis (Figure 8) of the deposited material. Figure 8 shows absorption peaks at 1453 and 1493 cm^{-1} related to C−C vibrations of the aromatic rings of the styrene monomers and another absorption at 1709 cm^{-1} attributed to C=O vibrations of the MA monomers of the adsorbed polymer.

Scanning electron microscopy (SEM) studies showed the formation of continuous and crack-free TiO_2−PSMA-h films
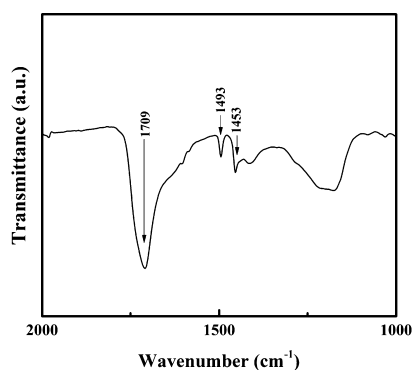
Figure 8. FTIR spectrum of a deposit, obtained from a suspension, containing 10 g L^{-1} TiO_2 and 10 g L^{-1} PSMA-h.

(Figure 9). It was found that the variation of TiO_2 concentration in the suspension resulted in changes of film
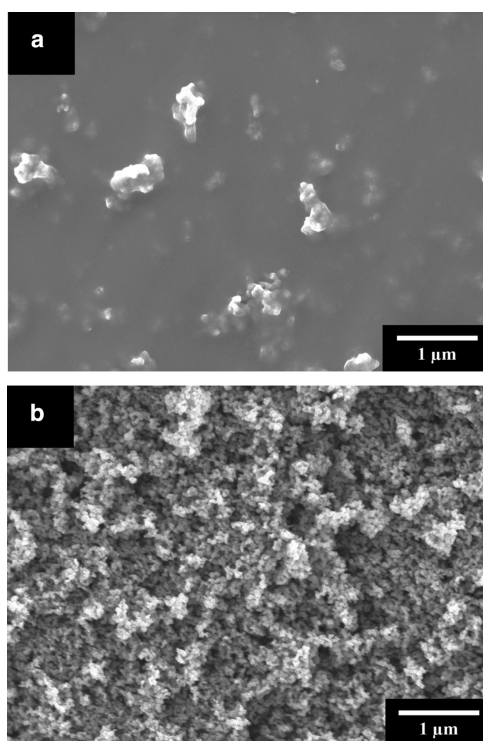
**Figure 9.** SEM images of deposits, prepared from (a) 5 and (b) 10 g L^{-1} TiO_2 suspension, containing 10 g L^{-1} PSMA-h at a deposition voltage of 10 V.

microstructure. The SEM image of a film prepared from 5 g L^{-1} TiO_2 suspension, containing 10 g L^{-1} PSMA-h showed TiO_2 particles in a PSMA-h matrix (Figure 9a). The SEM image of a film prepared from 10 g L^{-1} TiO_2 suspension (Figure 9b), containing 10 g L^{-1} PSMA-h, showed mainly TiO_2 particles, which formed a porous film. The film porosity resulted from the packing of TiO_2 particles. The comparison of the SEM images, shown in Figure 9a,b, indicated that the increase of TiO_2 concentration in the 10 g L^{-1} PSMA-h solution resulted in the increasing TiO_2 content in the deposited film.

The composite TiO_2−PSMA-h coating prepared from 5 g L^{-1} TiO_2 suspension, containing 10 g L^{-1} PSMA-h, was studied in Hank's balanced salt solution, which acted as a

simulated body fluid. Tafel plots comparing the electrochemical behavior of the coated and uncoated titanium are shown in Figure 10. From the Tafel plots, it can be seen that
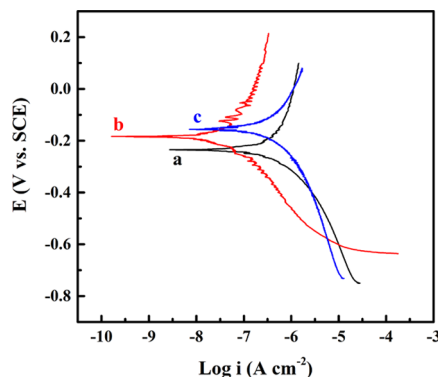
Figure 10. Tafel plots in Hank's solutions for (a) uncoated Ti, (b) coated by deposition from 5 g L^{-1} TiO_2 suspension, containing 10 g L^{-1} PSMA-h, and (c) coated by deposition from a suspension, containing 5 g L^{-1} TiO_2, 5 g L^{-1} HA, and 10 g L^{-1} PSMA-h at a deposition voltage of 10 V during 5 min.

the deposited TiO_2−PSMA-h coating allowed a reduction of the corrosion current, compared to an uncoated titanium. Moreover, the coated substrate showed a higher corrosion potential. These results demonstrated that the coating acted as a protective layer and provided corrosion protection of the titanium substrates. Therefore, the TiO_2−PSMA-h coating containing the bioactive TiO_2 rutile phase offers additional benefits of corrosion protection of underlying metallic substrates for biomedical implant applications.

Related to biomedical applications, we investigated PSMA-h as a codispersant for the codeposition of TiO_2 (rutile) and HA to fabricate composite rutile-HA coatings. A suspension containing 5 g L^{-1} HA, 5 g L^{-1} TiO_2, and 10 g L^{-1} PSMA-h was used for anodic EPD, and subsequent films were studied using XRD. The resulting XRD pattern is shown in Figure 11.
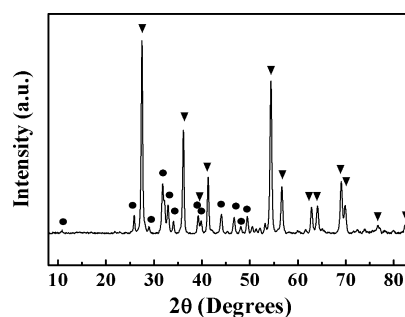
Figure 11. XRD pattern of a composite coating, prepared from a suspension, containing 5 g L^{-1} HA, 5 g L^{-1} TiO_2, and 10 g L^{-1} PSMA-h at a deposition voltage of 10 V (▼—TiO_2 rutile, ●—HA).

The XRD pattern showed TiO_2 (rutile) peaks, corresponding to the JCPDS file 021-1276, and peaks of HA, corresponding to the JCPDS file 046-0905. This confirmed that HA and TiO_2 were codeposited using PSMA-h, and thus composite HA-rutile-PSMA-h films were formed. The results of SEM studies (Figure 12) provided additional evidence of the formation of composite coatings. The SEM image presented in Figure 12 shows needle-shaped HA particles in addition to the TiO_2 particles. Therefore, PSMA-h can be used as a codispersing and
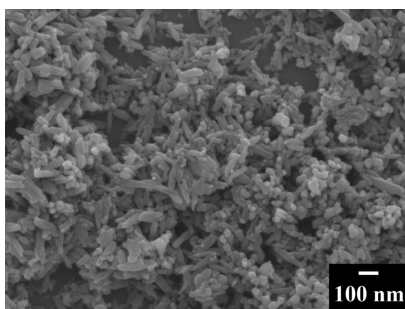
Figure 12. SEM image of the composite film, prepared from the suspensions, containing 5 g L^{-1} TiO$_2$, 5 g L^{-1} HA, and 10 g L^{-1} PSMA-h.

film-forming agent for the codeposition of HA and rutile. The composite coatings showed corrosion protection of Ti substrates, as indicated (Figure 10) by the increase in the corrosion potential and the reduction of the corrosion current. As emphasized above, the composite coating containing HA and rutile offers many benefits for biomedical applications. The EPD method has many processing advantages, such as high deposition rate and possibility of uniform deposition on substrates of complex shape and high surface area.

Finally, we would like to comment on an interference between adsorption of MA and hydration of surface by chemisorption of water molecules that takes place under relevant experimental conditions. The hydration of metal oxides is governed by the following two-step reaction:

$$\equiv Me^{q+} + H_2O \rightleftharpoons \equiv MeOH^{q-1} + H^+(aq) \tag{4a}$$

$$\equiv O^{q-} + H^+(aq) \rightleftharpoons \equiv OH^{1-q} \tag{4b}$$
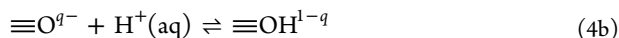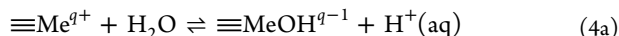
Here, $\equiv Me$ is a surface metal ion (either Ti or Ca) and q indicates its fractional charge. The charge is $q = 2/3e$ for the rutile (110) surface,[62] where e is the elementary charge. The HA($01\bar{1}0$) surface has several $\equiv Ca^{q+}$ and $\equiv O^{q-}$ sites with a range of q-values up to $1e$ due to a variety of dangling bonds created in the process of cleaving the surface (see Figure 2). The results for the enthalpy of water molecule chemisorption at these two surfaces are listed in Table 3. The water
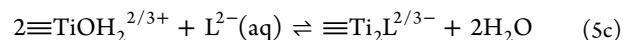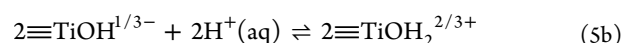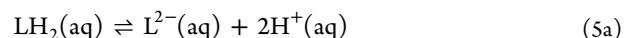
Table 3. Chemisorption Enthalpy of Water and MA Molecules at Rutile (110) and HA($01\bar{1}0$) Surfaces Calculated in the Gas Phase and in an Aqueous Solution

species	reactions	enthalpy (eV)	
		in the gas phase	aq. solution
H$_2$O on TiO$_2$	eq 4a	−0.9	−0.4
H$_2$O on HA	eq 4a	−1.8	+0.3
MA monomer on TiO$_2$	eq 5a		+0.3
MA segment on TiO$_2$	eq 5a		+0.4
MA monomer on HA	eqs 5a and 6a		−2.2
MA segment on HA	eqs 5a and 6a		−1.6

chemisorption is favorable at both surfaces in vacuum, which agrees with previous studies.[57,71] However, the presence of solvent not only reduces the magnitude of interaction but also changes the surface receptivity. As evident from Table 3, the enthalpy of dissociative adsorption of water molecules at the HA($01\bar{1}0$) surface in aqueous environment is positive, indicating that its chemisorption is unlikely. When reflected onto experimental conditions, this result implies that the
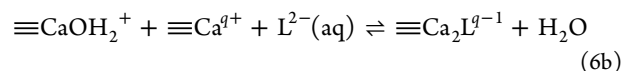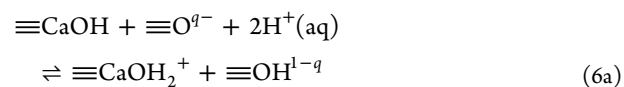
surface of rutile particles is likely to be terminated with hydroxyl groups during a reaction with PSMA-h, whereas the surface of HA is not. As a benchmark for the solvation model, we also computed the vaporization enthalpy of water molecule +0.32 eV versus the experimental value of +0.46 eV,[72] which sets error bars of the calculation.

Adsorption of MA on the rutile (110) surface in the presence of surface hydroxyl groups is described as a multistep ligand (L) exchange reaction:[4,73]

$$LH_2(aq) \rightleftharpoons L^{2-}(aq) + 2H^+(aq) \tag{5a}$$

$$2\equiv TiOH^{1/3-} + 2H^+(aq) \rightleftharpoons 2\equiv TiOH_2^{2/3+} \tag{5b}$$

$$2\equiv TiOH_2^{2/3+} + L^{2-}(aq) \rightleftharpoons \equiv Ti_2L^{2/3-} + 2H_2O \tag{5c}$$

which involves deprotonation of the ligand, protonation of surface hydroxyl groups on the Ti site, and finally the ligand exchange. This reaction leads to the desorption of two water molecules from the surface of TiO$_2$, which is energetically unlikely in an aqueous environment because of the reasons discussed in the preceding paragraph. As a result, an enthalpy is positive for the ligand exchange reaction between hydroxyl groups at the TiO$_2$ surface and MA monomer or MA segment as a part of PSMA-h (Table 3). To explain the experimentally observed adsorption of PSMA-h on TiO$_2$, we recall that the adsorption takes place in a water−ethanol solution. In their experimental study of adsorption of alcohols on the TiO$_2$ (rutile) surface, Suda et al.[74] noted that ethanol adsorption to the surface results in expelling water from the surface, which implies the presence of $\equiv Ti^{2/3+}$ bonding site at the surface with no need for the ligand exchange.

The absence of a strong dissociative bond between water and HA allows us to assume the coexistence of the hydrated $\equiv CaOH$ and $\equiv OH$ surface sites with unhydrated $\equiv Ca^{q+}$ and $\equiv O^{q-}$ sites. The ligand exchange reaction in this case proceeds through the following steps:

$$\equiv CaOH + \equiv O^{q-} + 2H^+(aq)$$
$$\rightleftharpoons \equiv CaOH_2^+ + \equiv OH^{1-q} \tag{6a}$$

$$\equiv CaOH_2^+ + \equiv Ca^{q+} + L^{2-}(aq) \rightleftharpoons \equiv Ca_2L^{q-1} + H_2O \tag{6b}$$

The corresponding enthalpy is strongly negative (see Table 3), indicating that, unlike in the case of TiO$_2$, there is no competition between water chemisorption and MA adsorption at the surface of HA.

4. CONCLUSIONS

PSMA-h adsorption on HA and TiO$_2$ (rutile) was studied using experimental techniques and corroborated by ab initio simulations of adsorption of a MA segment as a subunit of the copolymer. Ab initio calculations suggest that the MA segment adsorbs on the TiO$_2$ surface via an inner-sphere bridge bidentate bonding to a pair of Ti atoms. Chelation is a preferable type of bonding for the MA segment on HA due to peculiarities of the surface reconstruction. The aliphatic nature of MA makes it adaptive to various surfaces with a little energy penalty (on the order 0.15 eV) associated with structural changes such as flattening. The magnitude of the adsorption enthalpy for the MA monomer and the segment is comparable to that of catecholates. Solvent effects play a twofold role when providing quantitative evaluation of the adsorption energies

and thus cannot be neglected. First, it significantly reduces the adsorption strength (by almost a factor of 2 if compared to vacuum) as the polarity of the solvent increases. Second, a water chemisorption at the surface hinders the adsorption of MA at the surface of rutile. The results of first-principles calculations were confirmed by the experimental measurements. We found that adsorbed PSMA-h allowed efficient dispersion of rutile and formation of films by the EPD. We investigated the deposition yield and morphology of the films. Moreover, it was found that rutile can be codispersed and codeposited with HA to form composite films. The coatings obtained by the EPD showed corrosion protection of metallic implants in simulated body fluid solutions, which is a favorable characteristic for biomedical applications.

■ AUTHOR INFORMATION

Corresponding Authors
*E-mail: zhitom@mcmaster.ca. Phone: +1 905 5259140 ext. 24295 (I.Z.).
*E-mail: rubelo@mcmaster.ca (O.R.).

ORCID ⊕
Oleg Rubel: 0000-0001-5104-5602

Notes
The authors declare no competing financial interest.

■ REFERENCES

(1) Xu, A.-W.; Ma, Y.; Cölfen, H. Biomimetic mineralization. *J. Mater. Chem.* **2007**, *17*, 415−449.
(2) Lee, H.; Dellatore, S. M.; Miller, W. M.; Messersmith, P. B. Mussel-Inspired Surface Chemistry for Multifunctional Coatings. *Science* **2007**, *318*, 426−430.
(3) Lee, B. P.; Messersmith, P. B.; Israelachvili, J. N.; Waite, J. H. Mussel-Inspired Adhesives and Coatings. *Annu. Rev. Mater. Res.* **2011**, *41*, 99−132.
(4) Hidber, P. C.; Graule, T. J.; Gauckler, L. J. Influence of the dispersant structure on properties of electrostatically stabilized aqueous alumina suspensions. *J. Eur. Ceram. Soc.* **1997**, *17*, 239−249.
(5) Lee, H.; Lee, B. P.; Messersmith, P. B. A reversible wet/dry adhesive inspired by mussels and geckos. *Nature* **2007**, *448*, 338−341.
(6) Ata, M. S.; Liu, Y.; Zhitomirsky, I. A review of new methods of surface chemical modification, dispersion and electrophoretic deposition of metal oxide particles. *RSC Adv.* **2014**, *4*, 22716−22732.
(7) Clifford, A.; Ata, M. S.; Zhitomirsky, I. Synthesis, liquid - Liquid extraction and deposition of hydroxyapatite nanorod composites. *Mater. Lett.* **2017**, *201*, 140−143.
(8) Chen, R.; Ata, M. S.; Zhao, X.; Clifford, A.; Puri, I.; Zhitomirsky, I. Strategies for liquid-liquid extraction of oxide particles for applications in supercapacitor electrodes and thin films. *J. Colloid Interface Sci.* **2017**, *499*, 1−8.
(9) Poon, R.; Zhao, X.; Ata, M. S.; Clifford, A.; Zhitomirsky, I. Phase transfer of oxide particles for application in thin films and supercapacitors. *Ceram. Int.* **2017**, *43*, 8314−8320.

(10) Wallar, C.; Zhang, T.; Shi, K.; Zhitomirsky, I. Synthesis of metal and metal oxide nanoparticles, liquid-liquid extraction and application in supercapacitors. *Colloids Surf., A* **2016**, *500*, 195−202.
(11) Ye, Q.; Zhou, F.; Liu, W. Bioinspired catecholic chemistry for surface modification. *Chem. Soc. Rev.* **2011**, *40*, 4244−4258.
(12) Dobson, K. D.; McQuillan, A. J. In situ infrared spectroscopic analysis of the adsorption of aliphatic carboxylic acids to TiO2, ZrO2, Al2O3, and Ta2O5 from aqueous solutions. *Spectrochim. Acta, Part A* **1999**, *55*, 1395−1405.
(13) Lenhart, J. J.; Heyler, R.; Walton, E. M.; Mylon, S. E. The influence of dicarboxylic acid structure on the stability of colloidal hematite. *J. Colloid Interface Sci.* **2010**, *345*, 556−560.
(14) Pujari, S. P.; Scheres, L.; Marcelis, A. T. M.; Zuilhof, H. Covalent Surface Modification of Oxide Surfaces. *Angew. Chem., Int. Ed.* **2014**, *53*, 6322−6356.
(15) Gaponik, N.; Talapin, D. V.; Rogach, A. L.; Eychmüller, A.; Weller, H. Efficient Phase Transfer of Luminescent Thiol-Capped Nanocrystals: From Water to Nonpolar Organic Solvents. *Nano Lett.* **2002**, *2*, 803−806.
(16) Gao, X.; Tam, K.; Yu, K. M. K.; Tsang, S. C. Synthesis and Characterization of Thiol-Capped FePt Nanomagnetic Porous Particles. *Small* **2005**, *1*, 949−952.
(17) Paul, A.; Kaverina, E.; Vasiliev, A. Synthesis of silver/polymer nanocomposites by surface coating using carbodiimide method. *Colloids Surf., A* **2015**, *482*, 44−49.
(18) Mohanty, S.; Das, B.; Dhara, S. Poly(maleic acid) - A novel dispersant for aqueous alumina slurry. *J. Am. Ceram. Soc.* **2013**, *1*, 184−190.
(19) Blockhaus, F.; Séquaris, J.-M.; Narres, H. D.; Schwuger, M. J. Adsorption-Desorption Behavior of Acrylic-Maleic Acid Copolymer at Clay Minerals. *J. Colloid Interface Sci.* **1997**, *186*, 234−247.
(20) Zhao, J.; Wang, X.; Gui, Z.; Li, L. Dispersion of barium titanate with poly(acrylic acid-co-maleic acid) in aqueous media. *Ceram. Int.* **2004**, *30*, 1985−1988.
(21) Lai, C.-T.; Hong, J.-L. Role of Concentration on the Formulation of Zinc Oxide Nanorods from Poly(styrene-alt-maleic acid) Template. *J. Phys. Chem. C* **2009**, *113*, 18578−18583.
(22) Yu, J.; Tang, H.; Cheng, B.; Zhao, X. Morphological control of calcium oxalate particles in the presence of poly-(styrene-alt-maleic acid). *J. Solid State Chem.* **2004**, *177*, 3368−3374.
(23) Yu, J.; Guo, H.; Cheng, B. Shape evolution of SrCO3 particles in the presence of poly-(styrene-alt-maleic acid). *J. Solid State Chem.* **2006**, *179*, 800−803.
(24) Xu, A.-W.; Antonietti, M.; Yu, S.-H.; Cölfen, H. Polymer-Mediated Mineralization and Self-Similar Mesoscale-Organized Calcium Carbonate with Unusual Superstructures. *Adv. Mater.* **2008**, *20*, 1333−1338.
(25) Henry, S. M.; El-Sayed, M. E. H.; Pirie, C. M.; Hoffman, A. S.; Stayton, P. S. pH-responsive poly(styrene-alt-maleic anhydride) alkylamide copolymers for intracellular drug delivery. *Biomacromolecules* **2006**, *7*, 2407−2414.
(26) Dalela, M.; Shrivastav, T. G.; Kharbanda, S.; Singh, H. pH-Sensitive Biocompatible Nanoparticles of Paclitaxel-Conjugated Poly(styrene-co-maleic acid) for Anticancer Drug Delivery in Solid Tumors of Syngeneic Mice. *ACS Appl. Mater. Interfaces* **2015**, *7*, 26530−26548.
(27) Angelova, N.; Yordanov, G. Nanoparticles of poly(styrene-co-maleic acid) as colloidal carriers for the anticancer drug epirubicin. *Colloids Surf., A* **2014**, *452*, 73−81.
(28) Baghayeri, M.; Zare, E. N.; Namadchian, M. Direct electrochemistry and electrocatalysis of hemoglobin immobilized on biocompatible poly(styrene-alternative-maleic acid)/functionalized multi-wall carbon nanotubes blends. *Sens. Actuators, B* **2013**, *188*, 227−234.
(29) Samoilova, N.; Kurskaya, E.; Krayukhina, M.; Askadsky, A.; Yamskov, I. Copolymers of maleic acid and their amphiphilic derivatives as stabilizers of silver nanoparticles. *J. Phys. Chem. B* **2009**, *113*, 3395−3403.

(30) Saez-Martinez, V.; Punyamoonwongsa, P.; Tighe, B. J. Polymer-lipid interactions: Biomimetic self-assembly behaviour and surface properties of poly(styrene-alt-maleic acid) with diacylphosphatidyl-cholines. *React. Funct. Polym.* **2015**, *94*, 9−16.

(31) Hongkachern, T.; Champreda, V.; Srikhirin, T.; Wangkam, T.; Osotchan, T. Effect of pH on the formation of a bovine serum albumin layer on a poly(stryren-co-maleic acid) surface. *Adv. Mat. Res.* **2010**, *93−94*, 583−586.

(32) Clifford, A.; Luo, D.; Zhitomirsky, I. Colloidal strategies for electrophoretic deposition of organic-inorganic composites for biomedical applications. *Colloids Surf., A* **2017**, *516*, 219−225.

(33) Boccaccini, A. R.; Keim, S.; Ma, R.; Li, Y.; Zhitomirsky, I. Electrophoretic deposition of biomaterials. *J. R. Soc., Interface* **2010**, *7*, S581−S613.

(34) Cai, Y.; Li, H.; Karlsson, M.; Leifer, K.; Engqvist, H.; Xia, W. Biomineralization on single crystalline rutile: the modulated growth of hydroxyapatite by fibronectin in a simulated body fluid. *RSC Adv.* **2016**, *6*, 35507−35516.

(35) Lindahl, C.; Borchardt, P.; Lausmaa, J.; Xia, W.; Engqvist, H. Studies of early growth mechanisms of hydroxyapatite on single crystalline rutile: A model system for bioactive surfaces. *J. Mater. Sci.: Mater. Med.* **2010**, *21*, 2743−2749.

(36) Lu, X.; Zhang, H.-p.; Leng, Y.; Fang, L.; Qu, S.; Feng, B.; Weng, J.; Huang, N. The effects of hydroxyl groups on Ca adsorption on rutile surfaces: A first-principles study. *J. Mater. Sci.: Mater. Med.* **2010**, *21*, 1−10.

(37) Kasemanankul, P.; Witit-Anan, N.; Chaiyakun, S.; Limsuwan, P.; Boonamnuayvitaya, V. Low-temperature deposition of (110) and (101) rutile TiO2 thin films using dual cathode DC unbalanced magnetron sputtering for inducing hydroxyapatite. *Mater. Chem. Phys.* **2009**, *117*, 288−293.

(38) Xiao, X. F.; Liu, R. F.; Zheng, Y. Z. Characterization of hydroxyapatite/titania composite coatings codeposited by a hydro-thermal-electrochemical method on titanium. *Surf. Coat. Technol.* **2006**, *200*, 4406−4413.

(39) Ulasevich, S. A.; Kulak, A. I.; Poznyak, S. K.; Karpushenkov, S. A.; Lisenkov, A. D.; Skorb, E. V. Deposition of hydroxyapatite-incorporated TiO2 coating on titanium using plasma electrolytic oxidation coupled with electrophoretic deposition. *RSC Adv.* **2016**, *6*, 62540−62544.

(40) Jaworski, R.; Pawlowski, L.; Pierlot, C.; Roudet, F.; Kozerski, S.; Petit, F. Recent developments in suspension plasma sprayed titanium oxide and hydroxyapatite coatings. *J. Therm. Spray Technol.* **2010**, *19*, 240−247.

(41) Hannora, A. E.; Ataya, S. Structure and compression strength of hydroxyapatite/titania nanocomposites formed by high energy ball milling. *J. Alloys Compd.* **2016**, *658*, 222−233.

(42) Sarao, T. P. S.; Sidhu, H. S.; Singh, H. Characterization and In Vitro Corrosion Investigations of Thermal Sprayed Hydroxyapatite and Hydroxyapatite-Titania Coatings on Ti Alloy. *Metall. Mater. Trans. A* **2012**, *43*, 4365−4376.

(43) Kohn, W.; Sham, L. J. Self-Consistent Equations Including Exchange and Correlation Effects. *Phys. Rev.* **1965**, *140*, A1133−A1138.

(44) Perdew, J. P.; Burke, K.; Ernzerhof, M. Generalized Gradient Approximation Made Simple. *Phys. Rev. Lett.* **1996**, *77*, 3865−3868.

(45) Blöchl, P. E. Projector augmented-wave method. *Phys. Rev. B: Condens. Matter* **1994**, *50*, 17953−17979.

(46) Kresse, G.; Joubert, D. From ultrasoft pseudopotentials to the projector augmented-wave method. *Phys. Rev. B: Condens. Matter* **1999**, *59*, 1758−1775.

(47) Kresse, G.; Furthmüller, J. Efficient iterative schemes for ab initio total-energy calculations using a plane-wave basis set. *Phys. Rev. B: Condens. Matter* **1996**, *54*, 11169−11186.

(48) Monkhorst, H. J.; Pack, J. D. Special points for Brillouin-zone integrations. *Phys. Rev. B: Condens. Matter* **1976**, *13*, 5188−5192.

(49) Dudarev, S. L.; Botton, G. A.; Savrasov, S. Y.; Humphreys, C. J.; Sutton, A. P. Electron-energy-loss spectra and the structural stability

of nickel oxide: An LSDA+U study. *Phys. Rev. B: Condens. Matter* **1998**, *57*, 1505−1509.

(50) Hu, Z.; Metiu, H. Choice of U for DFT+U calculations for titanium oxides. *J. Phys. Chem. C* **2011**, *115*, 5841−5845.

(51) Howard, C. J.; Sabine, T. M.; Dickson, F. Structural and thermal parameters for rutile and anatase. *Acta Crystallogr., Sect. B: Struct. Sci.* **1991**, *47*, 462−468.

(52) Kay, M. I.; Young, R. A.; Posner, A. S. Crystal structure of hydroxyapatite. *Nature* **1964**, *204*, 1050−1052.

(53) Ramamoorthy, M.; Vanderbilt, D.; King-Smith, R. D. First-principles calculations of the energetics of stoichiometric TiO2 surfaces. *Phys. Rev. B: Condens. Matter* **1994**, *49*, 16721−16727.

(54) Bullard, J. W.; Cima, M. J. Orientation Dependence of the Isoelectric Point of TiO2(Rutile) Surfaces. *Langmuir* **2006**, *22*, 10264−10271.

(55) Zhu, W.; Wu, P. Surface energetics of hydroxyapatite: A DFT study. *Chem. Phys. Lett.* **2004**, *396*, 38−42.

(56) Almora-Barrios, N.; de Leeuw, N. H. A Density Functional Theory Study of the Interaction of Collagen Peptides with Hydroxyapatite Surfaces. *Langmuir* **2010**, *26*, 14535−14542.

(57) Chiatti, F.; Delle Piane, M.; Ugliengo, P.; Corno, M. Water at hydroxyapatite surfaces: the effect of coverage and surface termination as investigated by all-electron B3LYP-D* simulations. *Theor. Chem. Acc.* **2016**, *135*, 54.

(58) Mathew, K.; Sundararaman, R.; Letchworth-Weaver, K.; Arias, T. A.; Hennig, R. G. Implicit solvation model for density-functional study of nanocrystal surfaces and reaction pathways. *J. Chem. Phys.* **2014**, *140*, 084106.

(59) Wohlfarth, C. Dielectric constant of the mixture (1) water; (2) ethanol. In *Supplement to IV/6. Landolt-Börnstein − Group IV Physical Chemistry (Numerical Data and Functional Relationships in Science and Technology)*; Lechner, M. D., Ed.; Springer: Berlin, Heidelberg, 2008; pp 520−523.

(60) Bourikas, K.; Kordulis, C.; Lycourghiotis, A. Titanium Dioxide (Anatase and Rutile): Surface Chemistry, Liquid-Solid Interface Chemistry, and Scientific Synthesis of Supported Catalysts. *Chem. Rev.* **2014**, *114*, 9754−9823.

(61) Zhao, W.; Xu, Z.; Yang, Y.; Sahai, N. Surface Energetics of the Hydroxyapatite Nanocrystal-Water Interface: A Molecular Dynamics Study. *Langmuir* **2014**, *30*, 13283−13292.

(62) Zhang, T.; Wojtal, P.; Rubel, O.; Zhitomirsky, I. Density functional theory and experimental studies of caffeic acid adsorption on zinc oxide and titanium dioxide nanoparticles. *RSC Adv.* **2015**, *5*, 106877−106885.

(63) Gross, A.; Scheffler, M. Role of zero-point effects in catalytic reactions involving hydrogen. *J. Vac. Sci. Technol., A* **1997**, *15*, 1624−1629.

(64) Lee, H.; Scherer, N. F.; Messersmith, P. B. Single-molecule mechanics of mussel adhesion. *Proc. Natl. Acad. Sci. U.S.A.* **2006**, *103*, 12999−13003.

(65) Vega-Arroyo, M.; LeBreton, P. R.; Rajh, T.; Zapol, P.; Curtiss, L. A. Density functional study of the TiO2-dopamine complex. *Chem. Phys. Lett.* **2005**, *406*, 306−311.

(66) Bombarda, E.; Ullmann, G. M. pH-Dependent pKa Values in Proteins-A Theoretical Analysis of Protonation Energies with Practical Consequences for Enzymatic Reactions. *J. Phys. Chem. B* **2010**, *114*, 1994−2003.

(67) Pirrone, V.; Passic, S.; Wigdahl, B.; Rando, R. F.; Labib, M.; Krebs, F. C. A Styrene- alt -Maleic Acid Copolymer Is an Effective Inhibitor of R5 and X4 Human Immunodeficiency Virus Type 1 Infection. *J. Biomed. Biotechnol.* **2010**, *2010*, 548749.

(68) Zhitomirsky, I. Cathodic electrodeposition of ceramic and organoceramic materials. Fundamental aspects. *Adv. Colloid Interface Sci.* **2002**, *97*, 279−317.

(69) Ohshima, H. Electrophoretic mobility of soft particles. *Colloids Surf., A* **1995**, *103*, 249−255.

(70) Ohshima, H. Dynamic electrophoretic mobility of a soft particle. *J. Colloid Interface Sci.* **2001**, *233*, 142−152.

(71) Zheng, T.; Wu, C.; Chen, M.; Zhang, Y.; Cummings, P. T. A DFT study of water adsorption on rutile TiO2(110) surface: The effects of surface steps. *J. Chem. Phys.* **2016**, *145*, 044702.

(72) Cox, J. D.; Wagman, D. D.; Medvedev, V. A. *CODATA Key Values for Thermodynamics*; Hemisphere Publishing Corp.: New York, 1989.

(73) Rodriguez, R.; Blesa, M. A.; Regazzoni, A. E. Surface Complexation at the TiO2(anatase)/Aqueous Solution Interface: Chemisorption of Catechol. *J. Colloid Interface Sci.* **1996**, *177*, 122−131.

(74) Suda, Y.; Morimoto, T.; Nagao, M. Adsorption of alcohols on titanium dioxide (rutile) surface. *Langmuir* **1987**, *3*, 99−104.